Applied Catalysis B: Environmental 163 (2015) 16–22

Contents lists available at ScienceDirect

Applied Catalysis B: Environmental

journal homepage: www.elsevier.com/locate/apcatb

Construction of hybrid Z-scheme Pt/CdS–TNTAs with enhanced visible-light photocatalytic performance

Yuxiang Zhu[a,b,1], Zhi Chen[a,*,1], Tong Gao[a], Qiaoli Huang[a], Feng Niu[a], Laishun Qin[a], Peng Tang[b], Yuexiang Huang[a], Zuoliang Sha[b], Yanfei Wang[b,*]

[a] College of Materials Science and Engineering, China Jiliang University, No. 258 Xueyuan Street, Xiasha Higher Education District, Hangzhou 310018, Zhejiang Province, PR China

[b] Tianjin Key Laboratory of Marine Resources and Chemistry, College of Marine of Science and Technology, Tianjin University of Science and Technology, Tianjin, PR China

ARTICLE INFO

Article history:
Received 24 April 2014
Received in revised form 12 July 2014
Accepted 21 July 2014
Available online 30 July 2014

Keywords:
Z-scheme
Pt/CdS
TNTAs
Visible-light photocatalysis

ABSTRACT

Hybrid Z-scheme Pt/CdS–TNTAs nanostructures have been successfully fabricated through a simple route. Pt and CdS quantum dots (QDs) are homogeneously dispersed along the channels of TiO_2 nanotube arrays (TNTAs) and contact with TiO_2 support in a triangle form. Pt/CdS–TNTAs hybrid structure extends absorption into the visible-light region and presents enhanced activity of photocatalytic degradation of Rhodamine B under visible light, which is ascribed to the effective vectorial electron transfer of $CdS \rightarrow TiO_2 \rightarrow Pt$. It is proposed that superoxide and hydroxyl radicals should be the main active species in the photocatalytic reaction. Furthermore, the prepared catalyst has another advantage of easy recycling compared with the powder one.

1. Introduction

The environmental issue is an overwhelming problem around the world. In the past years, conventional biological and physical treatments have been used to remove the organic pollutants from wastewater [1–4]. The exploitation of pollution-free techniques for environmental remediation is an urgent task for the sustainable development. Semiconductor photocatalysis is a green methodology rapidly degrading organic pollutants with solar energy, and has attracted tremendous attentions [5,6]. Among the semiconductors, highly ordered TiO_2 nanotube arrays (TNTAs) are widely considered as the most promising and versatile material in dye-sensitized solar cells and photocatalysis. It has excellent controllability and stability as well as a large internal surface that can facilitate a fast rate of surface reactions. However, its further applications have been hindered by the low visible-light response and fast recombination of photo-generated electron–hole pairs [7–10].

Enormous efforts have been made to load noble metal or narrow-band-gap semiconductor quantum dots in the channels of TNTAs for improving the visible-light response and hampering the rapid recombination of photo-generated electrons and holes [11–25]. TNTAs structures decorated with Pd [12–14], Pt [15,16], Au [17], Ag [18,19], Cu_2O [20], CdS [21,22], CdTe [23], PbS [24] and WO_3 [25] have been previously explored for the enhancement of photocatalytic activity. CdS is a promising sensitizer for enhancing the visible-light response since it has a narrower band gap (2.40 eV) and a slightly higher conduction band level than TiO_2. Noble metal with a larger work function, meaning a lower Fermi level, should more readily trap electrons. Pt occupies the largest work function (5.65 eV) among the noble metals and is one of the promising cocatalysts for trapping electrons [26]. Recently, artificially Z-scheme photosynthetic system based on TNTAs has attracted striking interest since it consists of isolated photochemical system 1 (PS1), PS2 and the electron-transfer system [27]. The artificially photosynthetic system is considered as a simplified model to achieve high efficiency in light harvesting and spatial charge separation, wherein the key structural elements and key functions of natural photosynthesis could be reasonably mimicked [28,29]. Xie et al. firstly reported a ternary Z-scheme CdS/Ag–TNTAs system through an electrochemical deposition process according to the previously reported Z-scheme CdS–Au–TiO_2 based on TiO_2 particles [30,31]. Then, Wang and co-workers [32] deposited CdS nanoparticles in the same system by a successive ionic layer adsorption and reaction (SILAR) method. These results demonstrate that the three-component Z-scheme systems could have higher

* Corresponding authors. Tel.: +86 571 86875612; fax: +86 571 86875694.
E-mail addresses: zchen0@gmail.com (Z. Chen), wangyanfei@tust.edu.cn (Y. Wang).

[1] Yuxiang Zhu and Zhi Chen contribute equally to this work and should be considered as the co-first authors.

http://dx.doi.org/10.1016/j.apcatb.2014.07.041
0926-3373/

photocatalytic activity of degrading methylviologen or methylene blue than the single- and two-component systems. Park et al. prepared ternary CdS/TiO_2/Pt powder and found that the photocatalytic hydrogen production rate is as high as 6–9 × 10^{-3} mol h^{-1} g^{-1} and the deposition sequence has also influence on the photocatalytic performance [33]. Kang et al. [34] fabricated hybrid Z-scheme structure of CdS/Pt–TNTAs and observed higher bactericidal effect on *Escherichia coli* than single component. Nevertheless, the synthetic method was complicated and the loaded particles aggregated into large ones arbitrarily distributing on the surface of TNTAs. Moreover, the prepared ternary system demonstrated negative efficiency of charge transfer in comparison with the two-component system. Additionally, to the best of our knowledge, the application of Pt/CdS–TNTAs in the photocatalytic degradation of organic contaminant has not yet been reported.

Herein, we introduce a facile approach to construct ternary Z-scheme Pt/CdS–TNTAs nanostructure with enhanced visible-light photocatalytic performance. Pt and CdS quantum dots are uniformly deposited on the surface of TNTAs in sequence by a wet chemical method. The as-prepared samples are characterized and a structure model is proposed. Enhanced photocatalytic activity of visible-light degrading Rhodamine B (Rh B) is observed on Pt/CdS–TNTAs in comparison with pure TNTAs and single Pt or CdS QDs loaded sample, which indicates the presence of synergetic effects on Pt/CdS–TNTAs. The reaction mechanism on Pt/CdS–TNTAs is studied and the main active species should be superoxide and hydroxyl radicals. In addition, it is worth to mention that Pt/CdS–TNTAs catalyst has the advantage of easy recycling relative to TiO_2 powder catalyst since TiO_2 nanotube arrays are grown on the Ti foil.

2. Experimental

2.1. Synthesis

All chemicals, including glycerol (99.0% purity), $Cd(NO_3)_2$ (99.0% purity), $Na_2S{\cdot}9H_2O$ (98.0% purity), NH_4F (96.0% purity) and Ti foil (0.25 mm thick, 99.6% purity), were purchased from Sinopharm Chemical Reagent Co., Ltd and used without any further purification.

TNTAs film was fabricated by electrochemically anodizing Ti foils (2.0 cm × 5.0 cm) in a two-electrode electrochemical cell according to the literature [35]. Briefly, the anodization was performed by using Ti foil as the working electrode and Pt foil as the counter electrode at room temperature. Ti foil was firstly dipped in a acid solution ($HF:HNO_3:H_2O$ = 1/4/5, v/v/v ratio) for 1 min and degreased by 10 min ultrasonication in acetone, methanol and ethanol, respectively; then, it was rinsed with distilled water and dried in air prior to use. The cleaned Ti foil was anodized in 100 mL glycerol solution containing NH_4F (0.27 M) and H_2O (50 vol%, H_2O vs glycerol) at 20 V for 2 h (Fig. S1, Supplementary data). After anodization, TNTAs was annealed at 450 °C for 2 h to get crystalline anatase [35]. The main advantage of this technique is that nanotube arrays can be grown within a short time and the formed nanotubes are well adhered to the Ti substrate which benefits the recycling after catalytic process.

Pt QDs deposits were accomplished by a modified two-step photo irradiation-reduction method [36]. In this method, the platinum precursor solution (H_2PtCl_6, 38.62 mM) was preliminary irradiated for 45 min through an exposition to UV-light in the absence of TNTAs substrate. The resultant solution was diluted with ethanol/water (1/4, v/v) solution to get a precursor concentration of 0.5 mM. TNTAs films were rinsed with distilled water after soaked in the platinum solution for 16 h. Then, the samples were placed into a quartz vessel and irradiated for 30 min under air condition. Finally, Pt–TNTAs films were heated at 120 °C for 2 h in atmosphere. Compared with the traditional SILAR method for loading CdS QDs, Pt–TNTAs was alternately dipped into the solutions of 0.1 M $Cd(NO_3)_2$ and 0.1 M Na_2S in sequence for 1 min under magnetic stirring. The film was rinsed with distilled water to remove weakly adsorbed species after each dipping step. This operation was repeated several times until a desired deposition [37].

2.2. Characterizations

X-ray diffraction (XRD) was performed on Bruker Axs D2 PHASER diffractometer using Cu Kα as the radiation source. Raman spectra were measured on the Raman spectrometer (Horiba Jobin Yvon Co. Ltd.) using a 532 nm laser at a power of 0.25 mW. SEM images and elemental analyses were observed on Hitachi S-4800 field-emission scanning electron microscope (FE-SEM) attached an energy dispersive X-ray spectrometer (EDS). Transmission electron microscopy (TEM) and selected area electron diffraction (SAED) were operated on JEOL JEM-2100 field emission transmission electron microscopy at an accelerating voltage of 200 kV. UV–vis absorption spectra were obtained on a Shimadzu UV-3600 spectrophotometer equipped with an integrating sphere using $BaSO_4$ as the reference. Room-temperature photoluminescence (PL) spectra were recorded using a Hitachi High-Tech F-7000 fluorescence spectrophotometer with a xenon lamp as an excitation source (λ = 370 nm). X-ray photoelectron spectra (XPS) were recorded using a VG ESCALAB MK-2 spectrometer with Al Kα radiation (1486.6 eV). EPR signals of radicals trapped by DMPO were recorded at ambient temperature on a Bruker A300 spectrometer. The settings for the EPR spectrometer were as follows: center field, 3516 G; sweep width, 200 G; microwave frequency, 9.85 GHz; modulation frequency, 100 kHz; power, 20.20 mW.

2.3. Photocatalytic tests

The visible-light photo-degradations of Rh B dye on as-synthesized samples were evaluated by using a 300 W xenon lamp with a 420 nm cutoff filter as the light source. A square (1.5 cm × 2 cm) of prepared film was immersed into 20 mL Rh B aqueous solution at a concentration of 5 mg L^{-1} and the solution was agitated using a magnetic stirrer (Fig. S2, Supplementary data). As for the stability test, the film was taken out and rinsed with distilled water to remove the residual Rh B after one catalytic reaction. Then it was dried at room temperature before another catalytic reaction. This process was repeated for five times. Before light irradiation, Na_2S with a concentration of 0.02 M aqueous was added in the solution to compensate the photo corrosion of CdS similar with previous report. The absorbance of the testing solutions was measured at an interval of 0.5 h using a UV1700 UV-vis spectrophotometer to determine the decomposition rate of Rh B.

3. Results and discussion

3.1. Structure characterizations

As shown in Fig. S3 (Supplementary data), the XRD patterns clearly demonstrate that TNTAs before and after the modification with Pt, CdS and Pt/CdS are all anatase phase (JCDS, No. 21-1272). This indicates that no phase transition or structure destruction takes place during the deposition process. However, no obvious diffraction bands attributed to Pt or CdS are observed, suggesting that the loaded amount may be too low to be detected.

Raman spectra are employed to investigate the structure of the prepared sample, as shown in Fig. S4 (Supplementary data). Four peaks at 144, 394, 515 and 636 cm^{-1} can be assigned to the Raman

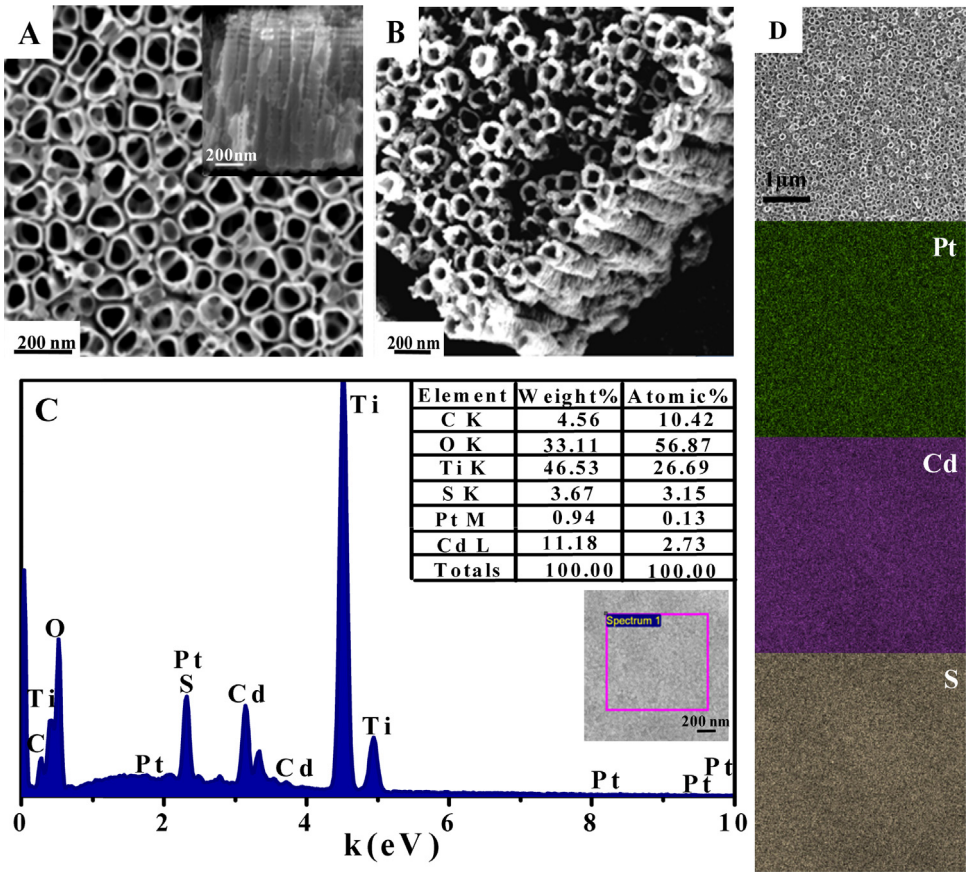

Fig. 1. FE-SEM images of (A) TNTAs and (B) Pt/CdS–TNTAs, (C) EDS spectrum of Pt/CdS–TNTAs, (D) SEM (top) and EDX mapping of Pt/CdS–TNTAs.

active modes $E_{g(1)}$, $B_{1g(1)}$, $B_{1g(1)}$ and $E_{g(3)}$ of anatase TiO_2, respectively [38]. This further confirms that the phase of TNTAs is anatase in correspondence with the XRD results. The $E_{g(1)}$ Raman peak of TNTAs (144 cm^{-1}) shows small shift in comparison with that of bulk anatase TiO_2 (147 cm^{-1}) due to the quantum size effect. New Raman peak at 303 cm^{-1} is observed on both CdS–TNTAs and Pt/CdS–TNTAs which can be indexed to the phonon (LO1) of CdS [37]. This verifies the formation and presence of CdS in Pt/CdS–TNTAs although no diffraction peaks of CdS are observed in XRD patterns.

FE-SEM images and EDX data of the prepared samples are shown in Fig. 1. As shown Fig. 1A, the average inner diameter of pristine self-organized TiO_2 nanotube is about 90 nm and the outer diameter is about 110 nm indicating that the nanotube has a wall thickness about 20 nm. A cross-sectional view of the film is shown in the inset indicating that the arrays are composed of well-aligned nanotubes with a length about 1 μm. Clear ripples are also observed along with the length direction and all the nanotubes grew vertically on the Ti substrate. As a contrast, SEM image of Pt/CdS–TNTAs is shown in Fig. 1B. Pt and CdS QDs are uniformly deposited onto the inside and outside walls and it can be clearly seen that the wall thickness of the nanotubes increases slightly after the decoration. The EDS data (from 1 μm × 1 μm area, as shown in the inset) of Pt/CdS–TNTAs are listed in Fig. 1C. The stoichiometric molar ratio of Cd/S is determined as 1:1, which further confirms the formation of CdS. The amount of Pt detected by EDS analysis is 0.13 at.% indicating that Pt and CdS QDs are successfully deposited in the channels of TNTAs. The detected amount of loaded species is low proving the above speculation that no detection of Pt or CdS from XRD analyses is resulted from the low loaded quantity. Pt, Cd and S element distribution maps of the region imaged on top Pt/CdS–TNTAs are shown in Fig. 1D. The elemental maps confirm the co-existence of Pt, Cd and S and prove that they are homogeneously dispersed on TNTAs.

TEM and SAED were employed to further investigate the microstructure of Pt/CdS–TNTAs, as shown in Fig. 2. From the low-magnification image (Fig. 2A), the ripples grown along with the channels of TiO_2 nanotube can be clearly seen, similar with the SEM results. Pt and CdS QDs are uniformly deposited on the nanochannel and the corresponding EDX analyses detect the presence of Cd, S and Pt, which confirms the results of SEM and XRD. Higher-magnification TEM image of the curved wall (part) is shown in Fig. 2B. It demonstrates that the wall thickness is about 20 nm which corresponds to the SEM result. The size of Pt (dark particles) and CdS (light ones) QDs are about 2 nm and 7 nm, respectively, determined with TEM images of Pt–TNTAs and CdS–TNTAs (Fig. S5, Supplementary data). The prepared particles are smaller than those of Kang et al. [34]. Selected area electron diffraction (SAED) pattern is shown in Fig. 2C and the diffractions of CdS (1 1 1), (2 0 0), (2 2 0) and Pt (1 1 1) are observed indicating that the presence of polycrystalline Pt and CdS. High-resolution TEM image (Fig. 2D) reveals the structure of three types of crystalline grains contacting with each other in triangle form. The observed lattice spacings are 0.35, 0.33 and 0.23 nm corresponding to (1 0 1) crystal plane of TiO_2, (1 1 1) plane of the cubic CdS and (111) plane of Pt, respectively. These results further prove that Pt and CdS QDs are both successfully deposited on TNTAs and interconnect with each other. XPS spectrum of Pt/CdS–TNTAs was also conducted and found that Pt species in these catalysts are predominantly oxidized, with very limited metallic Pt content, which should be resulted from the fact

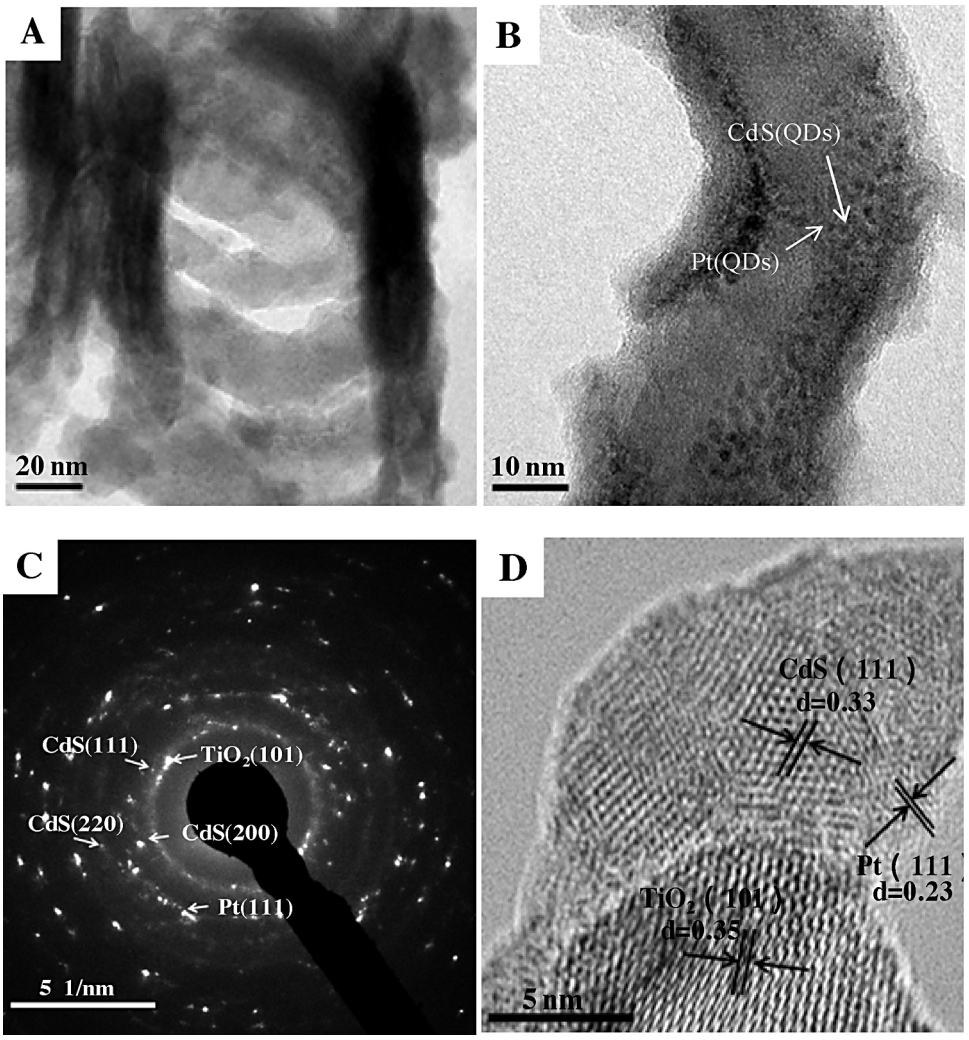

Fig. 2. TEM images of Pt/CdS–TNTAs at (A) low, (B) high magnification, (C) SAED patterns and (D) high-resolution.

that platinum ions were reduced by the photo irradiation-reduction method and the acquired catalysts were calcined at 120 °C (Fig. S6, Supplementary data).

UV–vis spectra are used to analyze the optical absorption of prepared samples, shown in Fig. 3A. Pure TNTAs can only absorb UV light and has a band gap of 3.27 eV, which is a little blue-shift comparing with that of bulk anatase (3.2 eV). This shift should come from the quantum size effect of small anatase nanocrystals which is in line with Raman analysis. However, strong absorptions in the visible-light region are observed on CdS–TNTAs and Pt/CdS–TNTAs. The calculated band gaps (inset of Fig. 3A) of CdS–TNTAs and Pt/CdS–TNTAs are 2.28 and 2.23 eV, respectively. This demonstrates that the loading of CdS or Pt/CdS can result in visible-light responses on TNTAs based material. The slight red shift between CdS–TNTAs and Pt/CdS–TNTAs, also Pt–TNTAs and TNTAs, should come from the electronic interaction among TNTAs, CdS QDs and Pt QDs [33,39].

PL emission spectrum has been widely used to investigate the lifetime of electron–hole pairs on semiconductor materials. Lower PL intensity suggests a lower density of recombination centers which consequently results in a longer lifetime of photo-generated carriers [30,40,41]. PL spectra of as-prepared TNTAs, Pt–TNTAs, CdS–TNTAs and Pt/CdS–TNTAs are exhibited in Fig. 3B. The PL intensity slightly decreases after the deposition of Pt QDs, indicating that there exits electron transfer between Pt and TNTAs, which suggests the formation of Schottky barrier. Further decrease of PL intensity is observed on CdS–TNTAs and Pt/CdS–TNTAs demonstrating that the modification of CdS and/or Pt QDs on TNTAs could reduce the recombination of photo-generated carriers. The drastic quenching of PL intensity on Pt/CdS–TNTAs states that there exists a remarkable electron interaction among Pt, CdS and TNTAs; which provides enhanced charge separation and synergetic effects in comparison with the single- and two-component systems.

3.2. Photocatalytic performance

Rh B can be found as a stable water contaminant from dying processes. The visible-light photodegradation of Rh B is employed to evaluate the photocatalytic activities of these catalysts. The characteristic absorption peak at 560 nm is used to determine the degradation degree of Rh B. The C/C_0 vs irradiation time is plotted in Fig. 4. As shown in the blank line, Rh B molecule is stable and experiences almost no decomposition in the absence of catalysts under the irradiation of visible-light, which excludes the possible self-degradation in the present system. After 150 min irradiation, the concentration of Rh B on pure TNTAs, Pt–TNTAs and CdS–TNTAs is reduced by about 18.15%, 23.15% and 30.35%, respectively. The photocatalytic activities on catalyst under visible-light is CdS–TNTAs > Pt–TNTAs > pure TNTAs which indicates that there exists electronic interaction between the loaded QDs and TNTAs substrate. In particular, Pt/CdS–TNTAs exhibits a much higher photocatalytic activity than CdS–TNTAs and Pt–TNTAs; and the

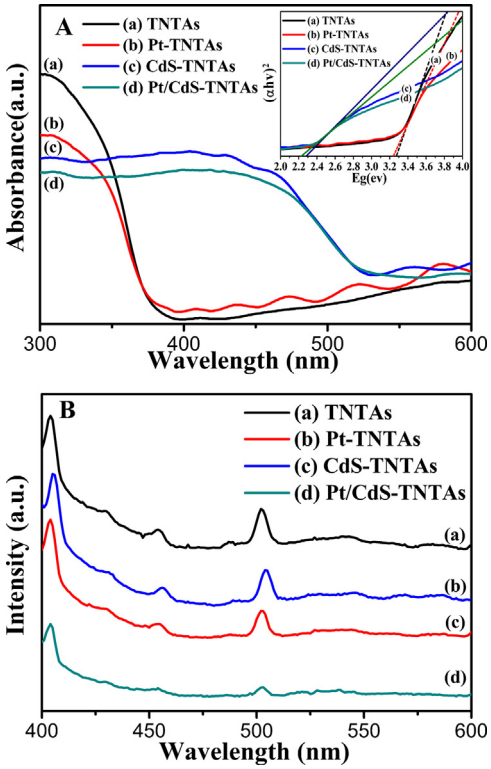

Fig. 3. UV–vis spectra (A) and PL response (B) of TNTAs, Pt–TNTAs, CdS–TNTAs and Pt/CdS–TNTAs.

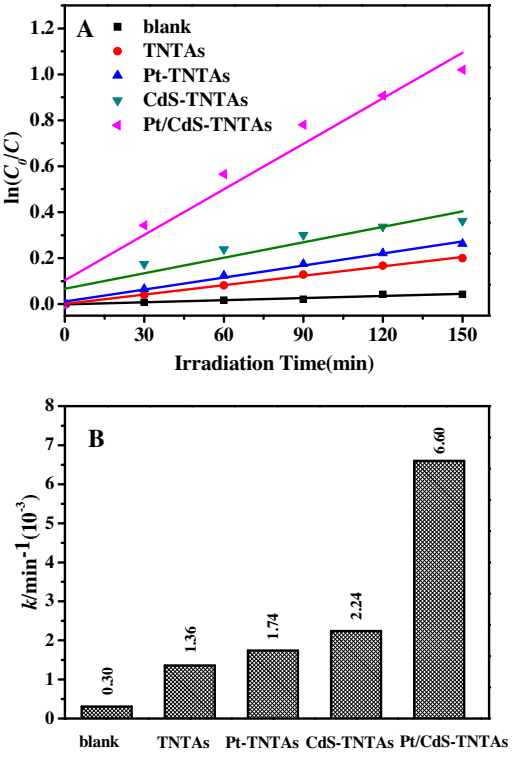

Fig. 5. (A) First-order kinetics data for the photodegradation of Rh B on TNTAs, Pt–TNTAs, CdS–TNTAs and Pt/CdS–TNTAs; (B) value of the rate constant k of the photodegradation of Rh B on TNTAs, Pt–TNTAs, CdS–TNTAs and Pt/CdS–TNTAs.

concentration of Rh B is reduced by nearly 63.93% after 150 min irradiation. This significant enhancement could be ascribed to the presence of synergetic effect, and this implies that vectorial electron transfer is driven by the two-step excitation of TiO_2 and CdS with Pt as a mediator [33,42]. As a comparison, Pt–CdS was also prepared according to previous report and the photo-degradation of Rh B was tested under the same condition as Pt/CdS–TNTAs (Fig. S7, Supplementary data). As shown, Pt/CdS–TNTAs demonstrates a much higher catalytic activity than that of Pt–CdS. It is worth noting that the net weight of a free standing nanotube layer excluded from Ti substrate is ≤1.6 mg and only one side of the prepared film is exposed to visible-light irradiation. It demonstrates that the prepared sample has a high visible-light photocatalytic performance.

To have a better understanding of the reaction kinetics of the Rh B degradation, the experimental data are fitted by a pseudo-first-order model. Fig. 5A shows the first-order kinetics data for the photodegradation of Rh B on the prepared samples. All fitting curves of $\ln(C_0/C)$ versus the irradiation time (t) are nearly linear. As shown in Fig. 5B, the rate constant (k) of Pt/CdS–TNTAs is apparently larger than those of single- or two-component systems, which is almost 5 times of pure TNTAs and 3 times of CdS–TNTAs. These results demonstrate that Pt/CdS–TNTAs may form the Z-scheme structure giving rise to synergetic effect and Schottky barrier, which play important roles in light harvesting and separation of photo-generated electron–hole pairs [28].

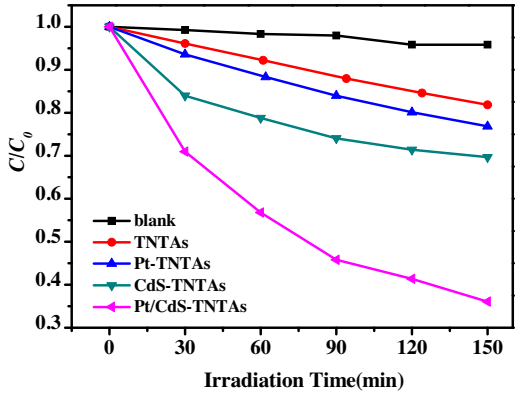

Fig. 4. Photocatalytic degradation of Rh B under visible-light irradiation on Pt–TNTAs, CdS–TNTAs and Pt/CdS–TNTAs.

3.3. Photocatalytic mechanism

A schematic mechanism is illustrated in Fig. 6 to interpret the enhanced photocatalytic activity in the Pt/CdS–TNTAs system. CdS, TiO_2 semiconductors and Pt metal interconnect with each other in a triangle form according to the above analyses. Once the narrow band-gap semiconductor CdS (PS1) and the wide band-gap semiconductor TiO_2 (PS2) are illuminated and activated simultaneously, the excited electron (e^-) quickly transfers from the CB of CdS through TiO_2 to noble metal Pt; whereas, holes (h^+) could accumulate in the VB of CdS, which is similar to the electron transfer process of natural photosynthesis system [32]. Electron transfers from the conduction band of TiO_2 to metal Pt, which results in the formation of a Schottky barrier. The Schottky barrier could effectively capture photo-generated electrons and reduce the rate of electron–hole recombination, which can improve the photocatalytic activity. Electrons arrived at Pt could react with adsorbed oxygen on the surface to generate super-oxide radicals ($O_2^{\bullet -}$). Simultaneously, a positive charged hole could react with OH^- or H_2O to form hydroxyl radicals ($^\bullet OH$). These two species are strong oxidant agents which can decompose organic agents such as Rh B.

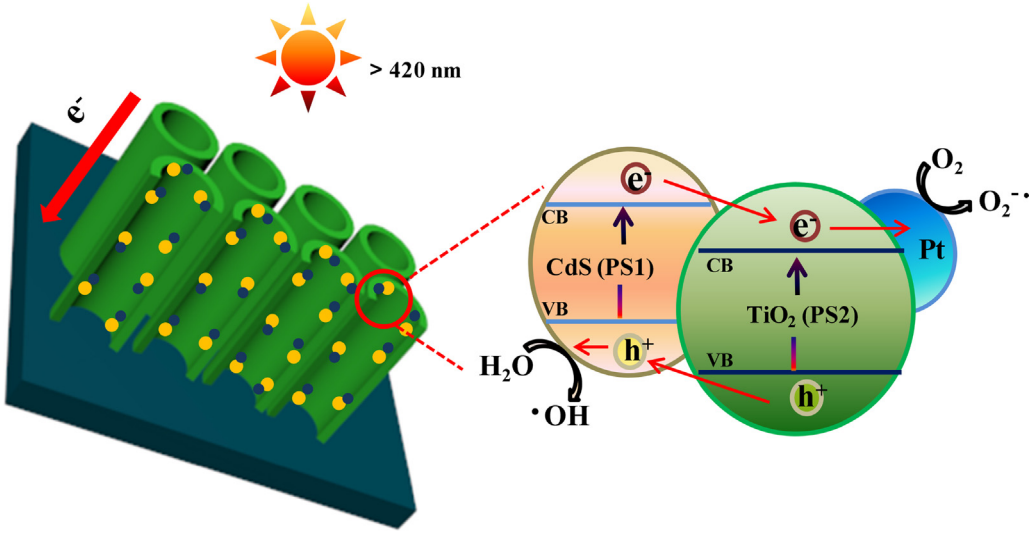

Fig. 6. Schematic diagram of Pt/CdS–TNTAs nanostructure and its charge transmission route.

In order to further reveal the visible-light photocatalytic mechanism on Pt/CdS–TNTAs, the trapping experiments were carried out to determine the main active species during the photocatalytic process. As illustrated in Fig. 7, the radical scavenger of tert-butyl alcohol (TBA, 2 mM) was added to trap hydroxyl radicals (•OH), while benzoquinone (BQ, 0.5 mM) was used to capture superoxide radicals ($O_2^{\bullet-}$), respectively [43,44]. As expected, once adding scavenger, the degradation of Rh B was significantly restrained, suggesting that the •OH and $O_2^{\bullet-}$ radicals should be both responsible for visible-light photocatalytic degradation. It is interesting to mention that the degradation behavior of Rh B was remarkably improved when disodium ethylenediaminetetraacetate (EDTA, 2 mM [45]), the holes scavenger, was added. This indicates that photo-generated holes might not be the main active species for the degradation of Rh B. The improved photocatalytic behavior should come from the fact that EDTA could effectively promote the separation of photo-generated electron–hole pairs.

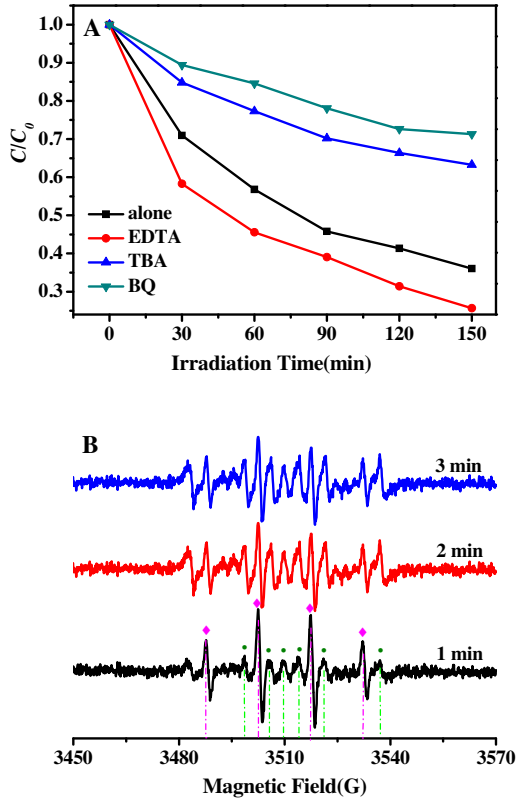

Fig. 7. (A) Photocatalytic degradation of RhB over Pt/CdS–TNTAs alone and with the addition of TBA, EDTA, and BQ; (B) EPR spectra of DMPO-•OH adducts and DMPO-$O_2^{\bullet-}$/HO_2• adducts.

EPR measurements have been conducted to further convince the above mentioned reaction radicals and the experiments were performed in deionized water solution containing a small amount of ethanol. As shown in Fig. 7B, the EPR spectra of Pt/CdS–TNTAs exhibited a typical four-peak spectrum with an intensity ratio of 1:2:2:1 (marked with the pink diamond symbol) which may come from the DMPO-•OH adducts. Besides, a typical six-peak signal of the DMPO-$O_2^{\bullet-}$/HO_2• adducts with an intensity ratio of 1:1:1:1:1:1 were also confirmed (marked with green dot symbol) [46]. The intensities of DMPO-$O_2^{-\bullet}$/HO_2• adducts were a bit lower than that of DMPO-•OH adducts which may result from the fact that the former is difficult to be scavenged in water solution. The intensities of DMPO-$O_2^{\bullet-}$/HO_2• adducts increased with the increase of irradiation time. These findings indicated that •OH and $O_2^{\bullet-}$ radicals were generated and involved in the decomposition process. Additionally, other peaks were also observed which are attributed to the noise signals from the oxidation of DMPO.

3.4. Catalytic stability of Pt/CdS–TNTAs

Repetitive experiments have been conducted to investigate the catalytic sustainability of Pt/CdS–TNTAs. Pt/CdS–TNTAs film was taken out and rinsed with distilled water to remove the residual Rh B after one catalytic reaction. Then it was dried at room temperature before another catalytic reaction. This process was repeated for five times. As can be seen in Fig. 8, the concentration of Rh B after the first cycle was reduced by 63.93% after 150 min irradiation; while it was reduced by about 59.02% at the fifth cycle with the same time irradiation. No significant loss of catalytic activity was observed after the fifth-cycle decomposition process. Accordingly, it can be concluded that Pt/CdS–TNTAs catalyst poses stability under specific condition.

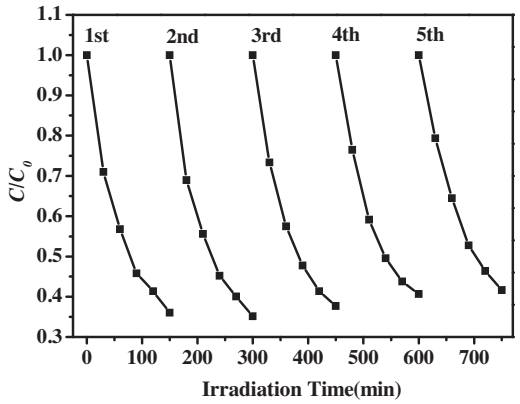

Fig. 8. Changes in the concentration of Rh B during the five-cycle decomposition process catalyzed by Pt/CdS–TNTAs.

4. Conclusions

In summary, Z-scheme Pt/CdS–TNTAs has been successfully prepared by simply depositing Pt and CdS QDs on the surface of TNTAs in sequence. Pt QDs about 3 nm and CdS QDs about 7 nm accumulate into the triangle form together with the TNTAs substrate. The resulting Z-scheme Pt/CdS–TNTAs has a strong visible-light response and presents synergetic effects and obvious electron interaction among these three components. Pt/CdS–TNTAs exhibits improved visible-light degradation of Rh B and shows more efficient charge transfer comparing with the single-component and two-component systems. The enhanced photocatalytic activity should be attributed to more efficient absorption of the visible-light and the effective separation of photo-generated carriers on Z-scheme system. The prepared samples are easy to be recycled after the catalytic process compared with powder catalysts; and no significant loss of catalytic activity was observed even after 5-cycles photo-degradation process. Besides, they have a high photocatalytic activity considering that the loaded quantity is low and only one side is exposed to irradiation. Moreover, the superoxide and hydroxyl radicals are responsible for the visible-light degradation of Rh B, which are also confirmed by EPR analysis. The prepared photocatalyst may have potential applications in environmental or other fields.

Acknowledgements

The authors greatly acknowledge Dr. Gao Tang at China Jiliang University for the contribution of the EPR analysis. This work is financially supported by International S&T Cooperation Program of China (No. 2013DFG52490) and the National Natural Science Foundation of China (No. 51372237).

Appendix A. Supplementary data

Supplementary data associated with this article can be found, in the online version, at http://dx.doi.org/10.1016/j.apcatb.2014.07.041.

References

[1] J. Ran, J. Zhang, J. Yu, M. Jaroniec, S.Z. Qiao, Chem. Soc. Rev. (2014), http://dx.doi.org/10.1039/c3cs60425j.
[2] C. Chen, W. Ma, J. Zhao, Chem. Soc. Rev. 39 (2010) 4206–4219.
[3] J. Bai, J. Li, Y. Liu, B. Zhou, W. Cai, Appl. Catal. B: Environ. 95 (2010) 408–413.
[4] Y.L. Pang, A.Z. Abdullah, Appl. Catal. B: Environ. 129 (2013) 473–481.
[5] S.P. Albu, A. Ghicov, S. Aldabergenova, P. Drechsel, D. LeClere, G.E. Thompson, J.M. Macak, P. Schmuki, Adv. Mater. 20 (2008) 4135–4139.
[6] C.N. Rao, A.R. Govindaraj, Adv. Mater. 21 (2009) 4208–4233.
[7] R. Asahi, T. Morikawa, T. Ohwaki, K. Aoki, Y. Taga, Science 293 (2001) 269–271.
[8] H. Tong, S. Ouyang, Y. Bi, N. Umezawa, M. Oshikiri, J. Ye, Adv. Mater. 24 (2012) 229–251.
[9] Y.Y. Song, F. Schmidt-Stein, S. Bauer, P.J. Schmuki, Am. Chem. Soc. 131 (2009) 4230–4232.
[10] M. Ye, D. Zheng, M. Lv, C. Chen, C. Lin, Z. Lin, Adv. Mater. 25 (2013) 3039–3044.
[11] A. Kudo, Y. Miseki, Chem. Soc. Rev. 38 (2009) 253–278.
[12] P. Roy, S. Berger, P. Schmuki, Angew. Chem. Int. Ed. 50 (2011) 2904–2939.
[13] M. Ye, J. Gong, Y. Lai, C. Lin, Z.J. Lin, Am. Chem. Soc. 134 (2012) 15720–15723.
[14] Z. Zhang, Y. Yu, P. Wang, ACS Appl. Mater. Interfaces 4 (2012) 990–996.
[15] C. Zhang, H. Yu, Y. Li, Y. Gao, Y. Zhao, W. Song, Z. Shao, B. Yi, ChemSusChem 6 (2013) 659–666.
[16] S.G. Leonardi, D. Aloisio, N. Donato, P.A. Russo, M.C. Ferro, N. Pinna, G. Neri, ChemElectroChem 1 (2014) 617–624.
[17] N. Liu, K. Lee, P. Schmuki, Angew. Chem. Int. Ed. 52 (2013) 12381–12384.
[18] M.H. Jung, Y.J. Yun, M.J. Chu, M.G. Kang, Chemistry 19 (2013) 8543–8549.
[19] Y. Lai, H. Zhuang, K. Xie, D. Gong, Y. Tang, L. Sun, C. Lin, Z. Chen, New J. Chem. 34 (2010) 1335.
[20] S. Zhang, S. Zhang, F. Peng, H. Zhang, H. Liu, H. Zhao, Electrochem. Commun. 13 (2011) 861–864.
[21] W.T. Sun, Y. Yu, H.Y. Pan, X.F. Gao, J. Am. Chem. Soc. 130 (2008) 1124–1125.
[22] Y.Y. Song, Q.L. Zhuang, C.Y. Li, H.F. Liu, J. Cao, Z.D. Gao, Electrochem. Commun. 16 (2012) 44–48.
[23] J.A. Seabold, K. Shankar, R.H.T. Wilke, M. Paulose, O.K. Varghese, C.A. Grimes, K.S. Choi, Chem. Mater. 20 (2008) 5266–5273.
[24] Q. Kang, S. Liu, L. Yang, Q. Cai, C.A. Grimes, ACS Appl. Mater. Interfaces 3 (2011) 746–749.
[25] C.W. Lai, S. Sreekantan, Electrochim. Acta 87 (2013) 294–302.
[26] J.H. Yang, D. Wang, H.X. Han, C. Li, Acc. Chem. Res. 46 (2013) 1900–1909.
[27] R.C. Prince, Trends Biochem. Sci. 21 (1996) 121–122.
[28] F.Y. Wen, C. Li, Acc. Chem. Res. 46 (2013) 2355–2364.
[29] R.J. Abe, Photochem. Photobiol. C 11 (2010) 179–209.
[30] K. Xie, Q. Wu, Y. Wang, W. Guo, M. Wang, L. Sun, C. Lin, Electrochem. Commun. 13 (2011) 1469–1472.
[31] H. Tada, T. Mitsui, T. Kiyonaga, T. Akita, K. Tanaka, Nat. Mater. 5 (2006) 782–786.
[32] Q. Wang, X. Yang, D. Liu, L. Chi, J. Hou, Electrochim. Acta 83 (2012) 140–145.
[33] H. Park, W. Choi, M.R. Hoffmann, J. Mater. Chem. 18 (2008) 2379.
[34] Q. Kang, Q.Z. Lu, S.H. Liu, L.X. Yang, L.F. Wen, S.L. Luo, Q.Y. Cai, Biomaterials 31 (2010) 3317–3326.
[35] J.M. Macak, P. Schmuki, Electrochim. Acta 52 (2006) 1258–1264.
[36] Y.Y. Song, Z.D. Gao, P. Schmuki, Electrochem. Commun. 13 (2011) 290–293.
[37] D.R. Baker, P.V. Kamat, Adv. Funct. Mater. 19 (2009) 805–811.
[38] J. Su, X. Zou, G.D. Li, Y.M. Jiang, Y. Cao, J. Zhao, J.S. Chen, Chem. Commun. 49 (2013) 8217–8219.
[39] L. Sang, H. Tan, X. Zhang, Y. Wu, C. Ma, C.J. Burda, Phys. Chem. C 116 (2012) 18633–18640.
[40] Y. Yao, G. Li, Environ. Sci. Technol. 42 (2008) 4952–4957.
[41] S.K. Parayil, H.S. Kibombo, C.M. Wu, R. Peng, J. Baltrusaitis, R.T. Koodali, Int. J. Hydrogen Energy 37 (2012) 8257–8267.
[42] Z. Chen, Q. Gao, M. Ruan, Nanotechnology 18 (2007) 255607.
[43] N. Zhang, Y. Zhang, M.Q. Yang, Z.R. Tang, Y.J. Xu, J. Catal. 299 (2013) 210–221.
[44] T.B. Li, G. Chen, C. Zhou, Z.Y. Shen, R.C. Jin, J.X. Sun, Dalton Trans. 40 (2011) 6751–6758.
[45] M.S. Elovitz, U.V. Gunten, Ozone Sci. Eng. 21 (1999) 239–260.
[46] Y. Yao, L. Wang, L. Sun, S. Zhu, Z. Huang, Y. Mao, W. Lu, W. Chen, Chem. Eng. Sci. 101 (2013) 424–431.